1

Description of Diamondoids

Shortly after the 3D structure of diamond was determined, the German chemist Hermann Decker recognized the connection between diamond and saturated hydrocarbons with "the 6-ring system built out into the third dimension" and suggested the term "diamondoid" for such molecules [1]. As the spatial arrangement of the carbon atoms resembles the diamond crystal lattice, diamondoids can therefore be viewed as hydrogen-terminated nanometer-sized diamonds with distinctive properties determined by their sizes and topologies. The smallest diamondoid is adamantane (**AD**, Figure 1.1), which has a cage skeleton consisting of ten carbons. Formal addition of further isobutyl fragments to the **AD** parent structure in a cyclohexane ring-forming manner results in higher diamondoid homologues. Diamondoids are classified as lower and higher homologues: lower diamondoids have only one isomeric form and include **AD** ($C_{10}H_{16}$), diamantane (**DIA**, $C_{14}H_{20}$), and triamantane (**TRIA**, $C_{18}H_{24}$), while higher diamondoids start with tetramantane (**TET**, $C_{22}H_{28}$) and possess isomers. Among three possible **TET** isomers, one is chiral (**123TET**) and is viewed as the parent of a new family of σ-helicenes [2]. As the cage grows, the number of isomers increases and beginning from pentamantane (**PENT**) spreads into different molecular weight subgroups, i.e., **PENT** has nine isomers with the $C_{26}H_{32}$ formula and one isomer with the $C_{25}H_{30}$ formula. Some other hydrocarbons also satisfy the structural criteria of partial or complete superposition on the diamond lattice, e.g., cyclohexane and decalin, so diamondoids are more precisely defined as "hydrocarbons containing at least one adamantane unit wholly or largely superimposable on the diamond lattice" [3]. Due to this definition, higher diamondoids bridge the gap between saturated hydrocarbons and diamond and are sometimes called nanodiamonds (in plural form to differentiate them from heterogeneous mixtures of nanodiamond material obtained by chemical vapor deposition, detonation, or shock-wave techniques [4]).

The molecular symmetry of diamondoids also plays a role in their self-assembly, readily producing crystals or serving as nucleation centers for bigger nanomaterial architectures. The smallest diamondoid **AD** is highly symmetric (T_d point group), whereas symmetry is generally (but not always) reduced as the diamondoids become larger, e.g., **DIA** and **TRIA** belong to the D_{3d} and C_{2v} point groups, respectively.

The Chemistry of Diamondoids: Building Blocks for Ligands, Catalysts, Materials, and Pharmaceuticals, First Edition. Andrey A. Fokin, Marina Šekutor, and Peter R. Schreiner.

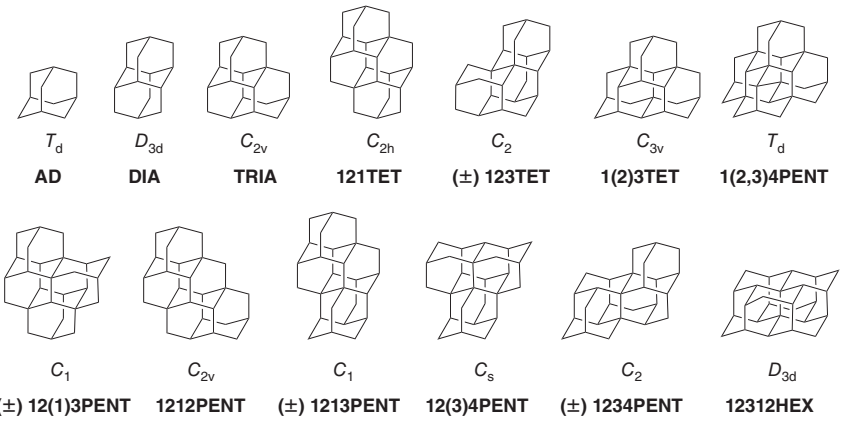

Figure 1.1 Structures and symmetry of diamondoid homologues up to cyclohexamantane (**12312HEX**).

Isomers of the first higher diamondoid **TET** display C_{2h} (**121TET**), C_2 (**123TET**), and C_{3v} (**1(2)3TET**) symmetry (Figure 1.1).

Note that **TET**s exemplify a common occurrence for higher diamondoids: different isomers have markedly different symmetries, which can be useful in material design by tailoring both the solubility of the material and the shape of the used building blocks. Moreover, diamondoids have one important advantage over bulk diamonds: they are "knowable," that is, their shapes are precisely determined by their molecular structure (rods, disks, helices, prisms, pyramids, cubes, etc.; Figure 1.2) and stoichiometry, and they can be obtained in homogeneous forms because they are single-molecule, nanometer-scale-sized building blocks. For instance, **DIA** and **121TET** are rod-shaped nanodiamond particles, **TRIA** and **1212PENT** have triangular shape, **1(2,3)4PENT** and **1231241(2)3DEC** are tetrahedron and cube, respectively, and **1(2)3TET** and **12312HEX** are prisms.

According to the definition of polymantanes, face-fused **AD** cage structures that are the focus of this book are not the only existing diamondoids. For example, **AD** dimers and higher single-bonded oligomers also belong to the class of diamondoid hydrocarbons (Figure 1.3). The first step in determining whether a saturated hydrocarbon belongs to the class of polymantane compounds is to check whether it has at least one **AD** subunit. If yes, then the next condition is that all cage atoms of the molecule need to be part of an **AD** unit; if that is also true, then the final condition is that two or more **AD** cages need to have at least six common carbon atoms, meaning that they share one face. When these conditions are met, a structure can be classified as a true diamondoid (Figure 1.3) [3].

1.1 Nomenclature

Before going further, we first define the diamondoid classification and nomenclature. As can be anticipated, von Baeyer's IUPAC names for these polycyclic

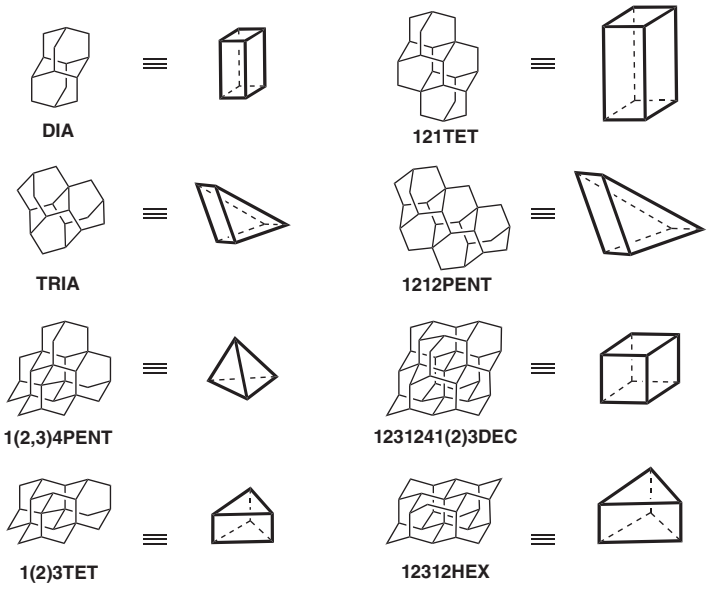

Figure 1.2 Structures of selected diamondoids linked to their geometrical representations. Source: Adapted from Ref. [5].

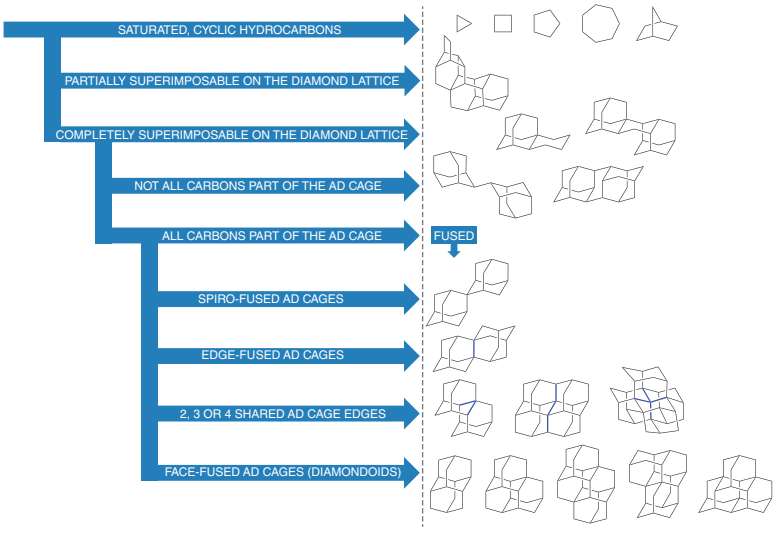

Figure 1.3 Classification of polymantanes.

compounds become quite cumbersome, and precise structural assignments require representing such molecular structures in terms of planar graphs [6]. Note that some programs, such as ChemDoodle, are quite useful for automatic IUPAC naming. As the cages grow larger and become more complex, the need to develop a special nomenclature for diamondoids emerges [3]. The initially proposed

graph-theory-based diamondoid classification and nomenclature [7] is still in use today and is termed the Balaban–Schleyer nomenclature (vide infra). As for the naming, the smallest representative **AD** is the basis: numerical multipliers indicate the number of fused **AD** subunits and are followed by adding the *-amantane* suffix, e.g., **DIA**, **TRIA**, and **TET**. Note, however, that starting from **TET** different isomers emerge, and they also need to be defined unambiguously. For this purpose, a dualist graph construction is used that gives the codes for specific stereoisomers and avoids confusing and non-systematic designations. For example, three possible isomers of **TET** are sometimes called *anti*-**TET** (C_{2h}-symmetry), *skew*-**TET** (chiral, enantiomeric pair, and C_2-symmetry), and *iso*-**TET** (C_{3v}-symmetry). However, this naming is based on their apparent geometrical shape and can hardly be transferred to higher homologues. In contrast, when applying the dualist graph convention, the naming becomes **121TET** (former *anti*, now [121]tetramantane), **123TET** (former *skew*, now [123]tetramantane), and **1(2)3TET** (former *iso*, now [1(2)3]tetramantane) and is a system applicable for all cage sizes. Essentially, this Balaban–Schleyer system uses four-digit codes (1, 2, 3, and 4) for the tetrahedral directions of covalent bonds around an imaginary center (Figure 1.4). These code descriptors are generated as follows: the center of the first **AD** cage is connected with the adjacent **AD** moieties in one of the four possible directions (**AD** has four faces), center-to-center. This direction is assigned number 1; the process is repeated until all **AD** subunits are accounted for and the whole molecule is traced with such vectors.

The digits emerge from taking different directions along the cage scaffold and, in the end, give a unique code characteristic for the isomer in question. This code is placed in brackets before the name of the stereoisomer. For more complicated geometries, when the diamondoid structure contains a branch, the digit of the corresponding vector is placed in parentheses, and if there are more branches, they are separated by commas inside the parentheses. In the case of longer branches, the chains of the branch are placed inside parentheses but without comma separation. One immediately notices the elegance of the Balaban–Schleyer approach as we have [123]tetramantane (**123TET**) instead of nonacyclo [$11.8.1.0^{1,20}.0^{2,7}.0^{4,21}.0^{6,19}.0^{9,18}.0^{11,16}.0^{15,20}$]docosane, [121]tetramantane (**121TET**)

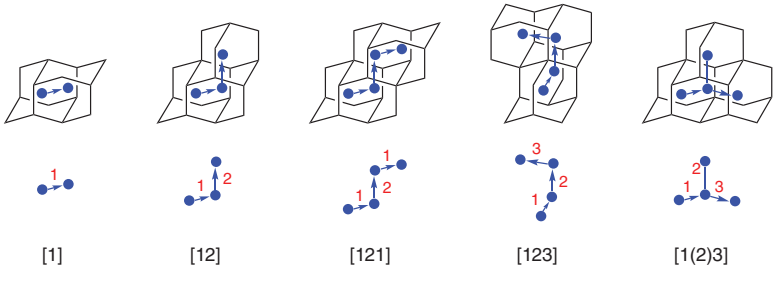

Figure 1.4 Examples of dualist graph construction for diamondoid naming suggested by Balaban and Schleyer.

instead of nonacyclo[11.7.1.1^{6,18}.0^{1,16}.0^{2,11}.0^{3,8}.0^{4,19}.0^{8,17}.0^{10,15}]docosane, [1212]pentamantane (**1212PENT**) instead of undecacyclo[11.11.1.1^{5,21}.0^{1,16}.0^{2,11}.0^{3,8}.0^{4,23}.0^{6,19}.0^{8,17}.0^{10,15}.0^{18,23}]hexacosane, and so on. Note that in the older literature, **DIA** is sometimes called "congressane" since it was proposed [8] as a synthetic challenge for the participants of the XIXth 1963 IUPAC meeting in London.

The dualist graph convention for the nomenclature of diamondoids enables a more straightforward way to designate diamondoid cages but as the cage size increases even such a naming system encounters complications. With increasing cage fusion, it becomes difficult to account for all possible stereoisomers and one way to resolve this type of complexity is to generate partitioned-formula tables based on the distribution of all the present carbon atoms according to them being quaternary (Q), tertiary (T), or secondary (S) [7a, 9]. By following this procedure, one obtains valence isomers of the same molecular formula $C_Q(CH)_T(CH_2)_S$ that are then shortened and denoted as Q – T – S, where the total amount of carbons is C = Q + T + S. For example, by using this convention, the formula for **AD** can be written as $(CH)_4(CH_2)_6$ or as 0–4–6, since the **AD** cage possesses no quaternary, four tertiary, and six secondary carbon atoms. Isomeric diamondoids with the same molecular formula, $C_Q(CH)_T(CH_2)_S$, can be divided into valence isomers by partitioning the number C into Q + T + S. Each [n]diamondoid has a dualist with n vertices and edges connecting vertices of adjacent **AD** units. Such a dualist is characterized by a quadruplet of indices (denoted as p, s, t, and q for primary, secondary, tertiary, and quaternary, respectively) specifying the connectivity of each vertex by assimilating it with a virtual carbon atom. Dualists help in classifying diamondoids as catamantanes with acyclic dualists, perimantanes with dualists having chair-shaped six-membered rings, or coronamantanes with dualists having only higher-membered rings.

An extension of the Schleyer–Balaban nomenclature that is more feasible for computer modeling was suggested recently [10]. This nomenclature is based on the numbering of centers of the diamond lattice starting from the origin (yellow, Figure 1.5) with further expansion along the chains and branches so that the structures can be systematically constructed. For instance, in accordance with this nomenclature, higher diamondoids [12312]hexamantane ($C_{26}H_{30}$), [121321]heptamantane ($C_{30}H_{34}$), and ([1 231 241(2)3]decamantane ($C_{35}H_{36}$) are now [1,2,3,6,7,18], [1,2,3,4,8,9,17], and [1,2,3,6,7,8,9,18,30] diamondoids that simplifies distinguishing and screening of large isomeric structures.

1.2 Strain

Strain reflects the electronic properties, and very recently it was found that the broad σ^*_{C-C} resonances in the near-edge X-ray absorption fine structure spectra of **AD** split into two narrow and intense resonances proportionally to the strain in a series from twistane and octahedrane to cubane [11]. It is often assumed that diamondoids are almost strain-free molecules, and indeed they are the most stable hydrocarbons of given brutto formulae. Strain can be seen as a relationship between

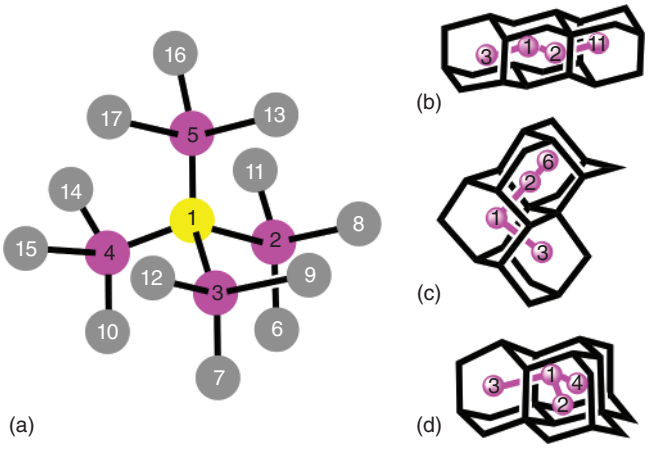

Figure 1.5 Nomenclature of diamondoids. (a) Parts of the diamond lattice with labeled numbers where the yellow atom represents the original atom and magenta and gray atoms are its first and second adjacent atoms, respectively; (b)–(d) are tetramantane isomers with numbering of their corresponding center atoms.

energy and structure that enables the evaluation of the structural feasibility of compounds. Straight-chain hydrocarbons in their linear, non-staggered conformations serve as the structural basis upon which strain is evaluated. Note, however, that even alkanes need not be absolutely strain-free but rather are taken as a point of reference for strain comparisons. Common criteria used when determining strain in structures are the presence of bond angles markedly deviating from the standard values, eclipsed conformations present in the structures, and atoms that approach each other too closely. Since the **AD** cage does not have these indicative features, it has long been considered strain-free (even though one should not forget about cyclohexane *gauche* interactions that lead to small strain, vide infra). While it is certainly true that diamondoids have little strain, there are some nuances to consider. Schleyer recommended using CH_3, CH_2, CH, and C group increments as well as force field calculations [12] for strain energy evaluations, in particular for diamondoids (Table 1.1) [13]. He concluded that the primary source of strain in diamondoids arises from slight deviations from the ideal C–C–C, C–C–H, and H–C–H angles when considering the cage angles where C–CH_2–C and C–CH–C fragments are interconnected. For instance, while the C–C–C angles in **AD** are 109.5°, these values are 112.4° and 111.3° in propane and isobutane, respectively. With size growing, the strain energy of diamondoids increases: it amounts to ca. 6 kcal mol^{-1} for **AD**, 11 and 13 kcal mol^{-1} for **DIA** and **TRIA**, respectively. However, the normalized strain energy (per carbon) remains almost constant (vide infra). Another source of strain is repulsive nonbonding C•••C interactions (akin to *gauche* interactions in *synclinal n*-butane and cyclohexane) throughout the cage itself. However, we also stress that 1,3-nonbonding intramolecular H•••H interactions are in fact acting beneficially due to London dispersion [14] (rediscovered much later as "protobranching" [15]) that is seen as an interplay

Table 1.1 Computed enthalpies of formation (gas) and strain energies (E_{str}) in kcal mol^{-1} for selected saturated hydrocarbons from molecular mechanics computations (EAS force field [12]).

Hydrocarbon	ΔH_f°	E_{str}
AD	−32.5	6.9
DIA	−37.4	10.7
TRIA	−44.4	13.4
Cyclopentane	−18.4	7.3
Cyclohexane	−29.4	1.4
Cycloheptane	−28.3	7.6
Cyclooctane	−29.2	11.9
Cyclononane	−30.7	15.5
Cyclodecane	−34.9	16.4
Norbornane	−13.0	17.0
ADAD	−53.7	21.5
Twistane	−13.3	26.1
Dodecahedrane	−0.2	43.0
Cubane	148.6	165.9

between medium-range correlation and steric repulsion [16]. The enthalpies of formation and evaluated strain energies for selected hydrocarbons presented in Table 1.1 are illustrative of the strain propagation in different cage molecules and are numerically still relevant [17] despite initially being computed using a simple Engler-Andose-Schleyer (EAS) force field method [12].

While the computational group equivalent approach is method-dependent [18], the errors largely cancel if homodesmotic equations are used [19]. The latter allows to compute the strain energies of hydrocarbons directly utilizing conventional strain-free references, such as ethane, propane, isobutane, and neopentane. This again gives the E_{str} of ca. 6 kcal mol^{-1} for **AD** (Eq. 1.1) and 2.2 kcal mol^{-1} for 1,3,5,7-tetramethyladamantane (**TMAD**) (Eq. 1.2) [15]. The fact that formally less crowded **AD** is more strained than **TMAD** may also be associated with additional electron delocalizations due to CC $\sigma \rightarrow \sigma^*$ hyperconjugation in the latter [20].

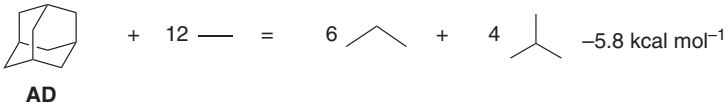

AD (1.1)

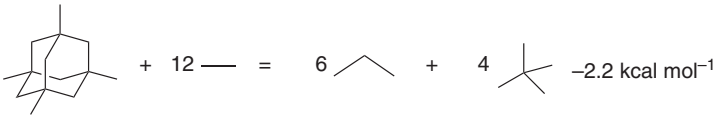

TMAD (1.2)

Table 1.2 Absolute (E_{str}) and normalized (per one carbon atom, E_{str}°) strain energies in kcal mol^{-1} of selected diamondoids $C_{4n+6}H_{4n+12}$ evaluated through homedesmotic equation $C_{4n+6}H_{4n+12} + k\ H_3CCH_3 = l\ H_3CCH_2CH_3 + m\ (CH_3)_3CH + p\ (CH_3)_4C$ at the B3LYP/6-31G(d) level (Source: From [21]).

Diamondoid	E_{str}	E_{str}°
AD	6.0	0.60
DIA	9.1	0.63
TRIA	10.8	0.60
121TET	12.3	0.56
1(2)3TET	11.5	0.52
123TET	17.5	0.79
1(2,3)4PENT	9.3	0.36
12312HEX	16.2	0.62

Computations predict [10, 21] the lowest values of the formation enthalpies for the most symmetric diamondoid structures. Accordingly, C_{3v}-tetramantane (**1(2)3TET**) and T_d-pentamantane (**1(2,3)4PENT**) are the most stable isomers. The strain energies of higher diamondoids were calculated utilizing Eq. 1.1, namely, $C_{4n+6}H_{4n+12} + k\ H_3CCH_3 = l\ H_3CCH_2CH_3 + m\ (CH_3)_3CH + p\ (CH_3)_4C$ at the B3LYP/6-31G(d) level [21]. The calculated strain energy of **DIA** (9.1 kcal mol^{-1}) and **TRIA** (10.8 kcal mol^{-1}) is higher than that for **AD** (6.0 kcal mol^{-1}); however, the normalized values (E_{str}°) are virtually identical to that of **AD** (ca. 0.6 kcal mol^{-1}, Table 1.2).

Additional strain in higher diamondoids may arise from destabilizing transannular HH contacts, such as in **123TET**, where some distances are ca. 2.1–2.2 Å (Figure 1.6); these are shorter than the sum of the van der Waals radii of two H-atoms (ca. 2.4 Å) [22], which causes destabilization of the structure. Such interactions are not present in **121TET** and **1(2)3TET,** which almost level their strain energies. Note that while the ideal tetrahedral **1(2,3)4PENT** is almost strain-free (0.36 kcal mol^{-1} per carbon), the strain energy of **12312HEX** (0.62 kcal mol^{-1} per carbon) is close to that of **AD**.

1.3 Preparation of Diamondoids

The construction of the **AD** core in tetraester (**TE**) was first achieved in 1937 by Oskar Böttger [23] through methylenation of Meerwein's ester (**ME**, Scheme 1.1) [24], readily available from formaldehyde and malonic ester [25]. The first successful synthesis of **AD** was achieved by Prelog [24, 26] as early as 1941, starting from **ME** through diester (**DE**) [27], however, with a very low yield (0.16% based on

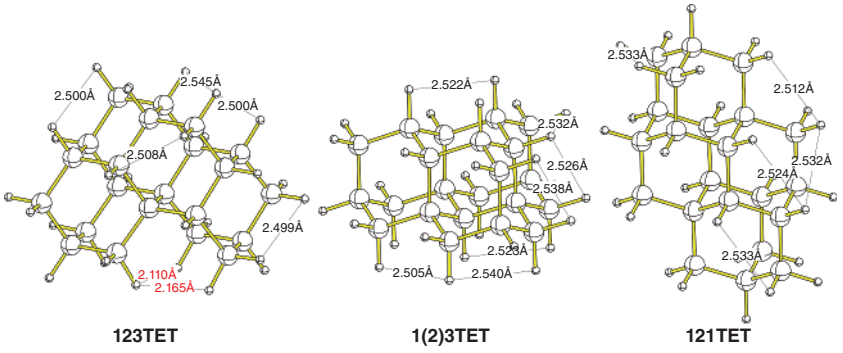

Figure 1.6 Additional strain in the *skew*-diamondoid **123TET** arose from several destabilizing transannular HH contacts (in red). The 1,3-HH contact distances of 2.5 Å are close to the sum of the van der Waals radii of two H-atoms (ca. 2.4 Å) and are stabilizing (protobranching).

ME). Further improvements of the decarboxylation steps, either through reductive decarboxylation of diacid **DA** [28] or tetraacid **TA** [29], utilizing the Hunsdiecker reaction, allowed for an increase in the overall yield of **AD** up to 1.5 and 6.5%, respectively. The bottleneck is the methylenation of **ME**, which determines the generally low yields. Schleyer, one of the most influential organic chemists of the twentieth century, simplified and perfected the synthesis of **AD** [30], making it available on an unprecedented large scale [31]. Schleyer's synthesis (Scheme 1.1, bottom) is based on the thermodynamically favorable Lewis acid-catalyzed rearrangement of tetrahydrodicyclopentadiene (**THCPD**) to **AD** [32]. Such "stabilomeric synthesis" not only made **AD** available in large quantities and thus significantly promoted the

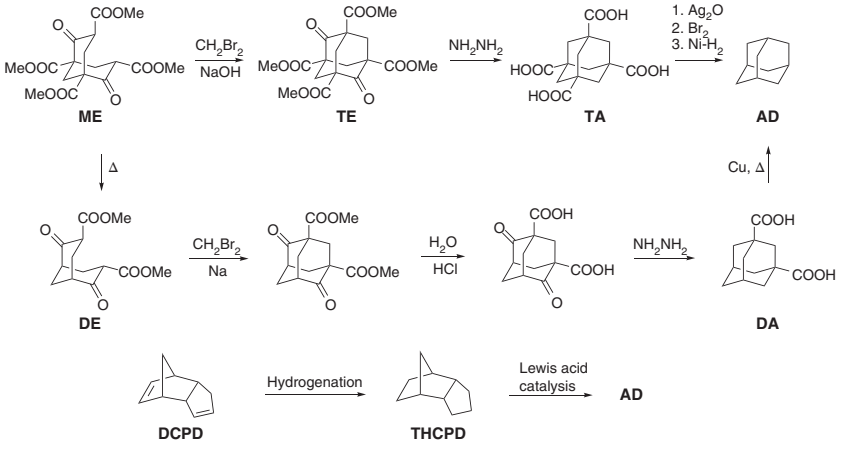

Scheme 1.1 Final steps in the synthesis of **AD** from Meerwein's ester (**ME**, top) and improved Schleyer's synthesis of **AD** from dicyclopentadiene (**DCPD**, bottom) through hydrogenation to tetrahydrodicyclopentadiene (**THCPD**) followed by Lewis acid-catalyzed rearrangement.

chemistry of cage compounds but also became very useful for the synthesis of larger polymantanes (vide infra).

The second diamondoid homologue, **DIA**, is also available synthetically and was first prepared by Schleyer and Cupas applying the same Lewis acid-catalyzed rearrangement procedure [8]. Photodimerization of norbornene afforded a cyclobutane-containing dimer **NBD**, which was treated with $AlCl_3$ and gave **DIA** (Scheme 1.2). As Schleyer noted [33], "Although the four-membered ring … was not ideal (too much strain in rearrangement precursors normally leads to ring opening and tar formation), I … suggested to Chris Cupas that he investigate the rearrangement. The first experiment failed but in the second experiment he noticed sublimed crystals on the cooler portion of the flask that proved to be congressane." This method unfortunately gave very low yields and produced a significant amount of tar, although it enabled X-ray analysis and confirmation of the **DIA** structure [34]. Schleyer further improved the synthesis to make it relevant for practical applications [35]. The modification included the use of a more efficient precursor, **Binor-S** [36], that, after hydrogenation and treatment with $AlBr_3$, gave **DIA** in a yield of over 60% for the last step (Scheme 1.2) [35, 37].

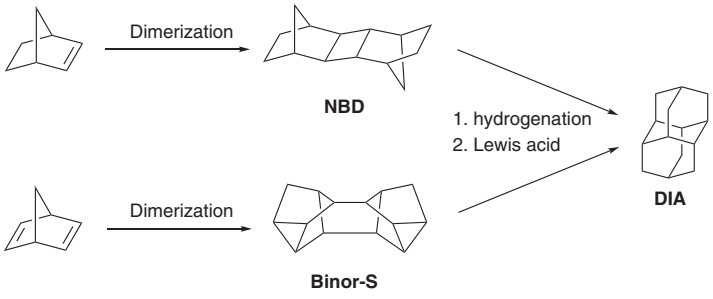

Scheme 1.2 First synthesis of **DIA** from the norbornene dimer (**NBD**) and multi-gram synthesis using **Binor-S** as a precursor.

Schleyer also prepared **TRIA** in a similar way from bis-cyclopropanated polycyclic dimer of cyclooctatetraene (**DCOT**) using the $AlBr_3$/*tert*-BuBr sludge catalyst [38]. Reductive cleavage of the cyclopropane rings followed by isomerization resulted in **TRIA**, albeit in a very low yield (under 5%) for the final step. McKervey made a slight improvement in **TRIA** synthesis by using **1COOHDIA** as a starting molecule that underwent cage rearrangement as the last step [39], and he could further improve the synthesis by using **Binor-S** heated on a platinum catalyst that gave cyclic olefins [40]. Diels–Alder reaction of these olefins with butadiene and Lewis acid-catalyzed rearrangement afforded the target hydrocarbon with satisfactory preparative yield (Scheme 1.3).

The attempt to expand the stabilomeric approach to the preparation of diamondoids higher than **TRIA** failed. In particular, the isomerization of $C_{22}H_{28}$ hydrocarbons derived from the hydrogenation of the Diels–Alder adduct of 1,3-cyclohexadiene with the 38.5 °C melting cyclooctatetraene dimer (**DCOT**) gave unwanted ethano-bridged isomer "bastardane" (**BAST**) rather than **121TET**

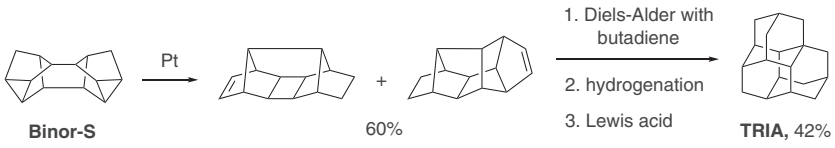

Scheme 1.3 Efficient synthesis of **TRIA** from **Binor-S** by McKervey.

(Scheme 1.4) [41]. Despite **BAST** being thermodynamically less stable than **121TET,** it is unreactive toward Lewis acids because further rearrangement is likely to involve unstable quaternary carbon intermediates.

Of the three possible **TET** isomers, only **121TET** has been successfully synthesized to date [42]. McKervey applied a ring expansion reaction on **DIA** 1,6-dicarboxylic acid (**16COOHDIA**) that resulted in cyclization to the isomeric polycyclic dienes that upon isomerization provided **121TET** (Scheme 1.4). The yield was, however, quite low (10%) but gave enough material to determine the X-ray crystal structure of the target hydrocarbon [43]. Later, it was noted that the final step of the reaction is highly sensitive to the variations in the temperature of the catalyst bed [44].

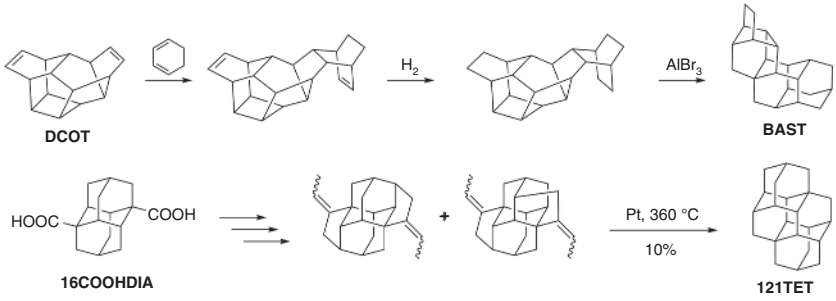

Scheme 1.4 An unsuccessful attempt to prepare **121TET** by stabilomeric synthesis (top) and multi-step synthesis from diamantane 1,6-dicarboxylic acid (**16COOHDIA**) by McKervey (bottom).

To date, no other diamondoid hydrocarbons aside from these four are available synthetically, although many attempts have been made to achieve this goal [45]. The reason is either in the presence of the "dead end" intermediates (like **BAST**) [41], or the increase in the number of isomers with similar thermodynamic stability as the cage size increases [45b, 46], meaning that the Lewis acid rearrangement procedure gives a complex mixture of products that cannot be easily separated.

However, there is a silver lining: diamondoids are readily available from nature! Since diamondoids are naturally occurring molecules that are formed by catagenesis in oil deposits, they can be isolated from mature crude oil, natural gas, and hydrocarbon-rich sediments, as described in Chapter 2. A historical curiosity is that **AD** was first isolated from an oil reservoir near Hodonin, Czechoslovakia, in 1933 [47] and was only later prepared synthetically [24, 28]. Other diamondoids are also present in oil [48] and may have been formed by Lewis acid-catalyzed rearrangement promoted by acidic minerals. The challenge is to harness them from complex oil

mixtures. A breakthrough came in 2003 when Dahl, Liu, and Carlson demonstrated that various diamondoids can indeed be individually separated from crude oil mixtures [49]. Note that until then diamondoids were a known unwanted issue in the oil industry: these hydrocarbons often caused problems in production since they clogged pipes and machinery during oil refinement as they had the tendency to condense and solidify on the cool equipment parts. This behavior comes as no surprise since diamondoids have moderate solubility and high melting points (e.g., 268 °C for **AD**, 237 °C for **DIA**, and 221 °C for **TRIA**), while at the same time they are very volatile and resistant to oxidation. These issues arising in the industrial processing of oil actually provide a clue for the isolation and purification of individual diamondoids. Dahl et al. took advantage of these solidification-inducing properties and separated 21 different diamondoids by using a combination of various purification methods and multiple high-performance liquid chromatography (HPLC) runs. In the end, derivatives ranging from **TET**s up to undecamantane were identified, and X-ray analyses were used to unambiguously confirm the structures of some of them (Figure 1.7) [49, 50]. Even though it has been known for a long time that lower diamondoids are present in oil [47, 51], the occurrence of higher diamondoids in oil deposits was finally unequivocally proven by this isolation endeavor.

As was already mentioned, the synthetic preparation of higher diamondoids by carbocationic rearrangements was not feasible due to many possible isomeric structures that are often energetically comparable, thus leading to reaction pathways where the intermediates become trapped in local energy minima, resulting in the formation of many unwanted side products. However, we saw that higher diamondoids exist in oil, and they are thermodynamically the most stable hydrocarbons, meaning that their chemical synthesis in the laboratory simply must be possible.

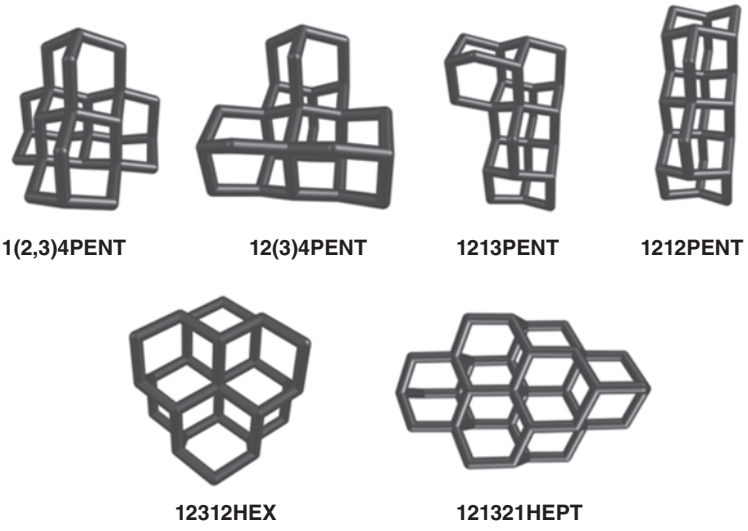

Figure 1.7 Structures of higher diamondoids obtained from X-ray crystal analyses [49, 50]. Hydrogens were omitted for clarity.

Inspired by this rationale, a groundbreaking preparative procedure has been developed that provides synthetic access to the higher homologs [52]. Since diamondoids form in oil that has undergone thermal cracking, the suggestion was that free-radical cracking reactions are an alternative to the proposed acid-catalyzed carbocationic rearrangements. Astonishingly, upon mimicking the reaction conditions that are present during cracking processes, **TET** and **PENT** isomers form when **TRIA** is subjected to sealed tube pyrolysis experiments. The obtained amounts were small, and alkylated **TRIA** derivatives were the predominant products; however, this experiment provided an excellent proof-of-principle that radical pathways must not be disregarded for diamondoid generation. Similarly, **PENT** isomers could be produced from **TET**s using the same procedure, and the most favored stereoisomers were those with the least steric crowding (Figure 1.8).

In addition, **PENT** isomers that require breaking and reconstruction of the parent **TET** cage were disfavored. This finding strongly implies that the parent diamondoid cage actively directs further cage growth and that only surface hydrogens are involved in the bond construction process. The addition of isobutene

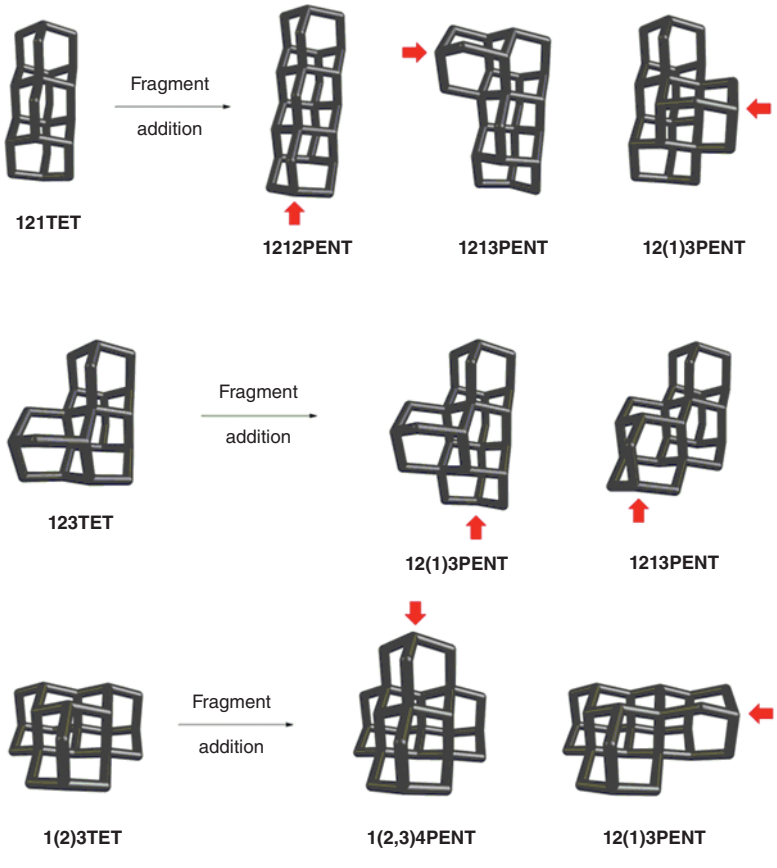

Figure 1.8 Preferred cage growth from the initial tetramantane isomers from the least crowded apical positions of the cage. Hydrogens were omitted for clarity.

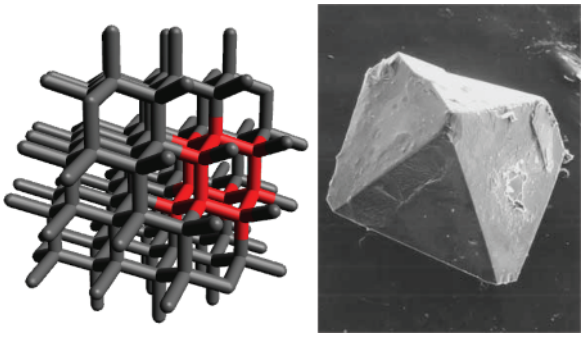

Figure 1.9 Cutout from the crystal lattice of diamond with the superimposed structure of the **AD** cage (red) and SEM image of a **12312HEX** crystal magnified 150 times. Hydrogens were omitted for clarity. Source: Reproduced from Ref. [50], Wiley-VCH, 2003.

greatly improved the reaction yields since the isobutyl moiety is essentially all that is needed for the construction of the next cage. What is still unclear is the exact mechanistic pathway for this ring closure because it is possible that introduced isobutyl sources form either free radicals that add one carbon atom at a time or form isobutyl radicals that add directly to the cage. The merit of the described sequential cage construction lies in the preparation of microcrystalline diamond: by using large diamondoids as seeding centers, it is possible to trigger nucleation and diamond growth akin to chemical vapor deposition methods [52].

Another approach to prepare higher diamondoids is by using a plasma and a supercritical medium as the solvent, either xenon [53] or carbon dioxide [54]. When **AD** is used as a precursor and a seeding center, a mixture of higher diamondoids typically forms (see Chapter 6 for more details). The obtained reaction products were analyzed spectroscopically and compared with pure samples where available, e.g., **12312HEX** [53a]. An in-depth monograph has recently been published describing the use of plasma for diamondoid generation, and we refer the interested reader to that work [55].

Since nanodiamonds have the spatial arrangement of their cage carbon atoms superimposable on the diamond crystal lattice (Figure 1.9), diamondoids are at the core of nanoscience [56]. Their properties make them promising materials of the future, side by side with graphene, carbon nanotubes, and other carbon-based entities.

1.4 Physical Properties of Diamondoids

The solubility of diamondoids in organic solvents correlates with their size, shape, and symmetry. A practical rule of thumb for diamondoids is that their solubility drops as their size increases. For instance, the solubility of **12312HEX** in organic solvents is so low that it initially caused difficulties in measuring the ^{13}C NMR spectrum of this hydrocarbon [5, 50]. For diamondoids of approximately the same size, symmetry also needs to be taken into account because the higher the cage symmetry is, the more difficult it is for the solvent molecules to solubilize and remove the molecules from the solid state. For example, the solubility of apically substituted **DIA** derivatives with axial symmetry is lower than that of the analogously

substituted medial compounds. As expected, the parent hydrocarbons have higher solubility in nonpolar solvents (Figure 1.10) [57], but it is lower than that of other alicyclic hydrocarbons. As previously mentioned, poor diamondoid solubility and high volatility often cause technical difficulties in oil refinement since they are prone to clogging pipes when present in substantial amounts due to continuous processing.

Nanotechnological diamondoid applications require highly pure starting materials. Commonly used procedures for diamondoid purification include multistage distillation or HPLC [49]. Despite being effective, both methods have some drawbacks from ecological and economical points of view: the former consumes large quantities of energy, while the latter uses large amounts of organic solvents. In addition, HPLC purification suffers from the problem of having to use a suitable detector because diamondoid solutions are not easily detectable with common HPLC analyzers. This leaves the differential refractive index as the only option for detection, but it is three to four orders of magnitude less sensitive than other common detectors. These purification issues were addressed and circumvented by using vapor transport techniques to grow large diamondoid single crystals [58]. The process enables efficient growth of crystals up to around 1 cm^3 (Figure 1.11) under mild conditions without using organic solvents because diamondoids readily form ordered crystals at room temperature, a feature not common for other saturated hydrocarbons. Moreover, with their relatively high vapor pressures, diamondoids can easily sublime. Thus, single crystal growth of diamond molecules through the vapor phase is a viable and effective method for diamondoid purification, a technique that can readily be controlled by temperature manipulation.

Other physical and chemical properties of diamondoid cages that are a direct consequence of their diamond-like structure include high lipophilicity, structural rigidity, thermodynamic stability, high melting points, and facile crystallization [32]. Their often encountered high symmetry can also aid in their structural characterization, as Raman and IR spectroscopies are often a method of choice for analyzing saturated hydrocarbons [59]. In addition to assigning the obtained spectral peaks to their vibrational modes, vibrational spectroscopy is also useful for in-depth analysis of bulk materials and for studying phase changes of diamondoid self-assemblies. As diamondoids are typically available as micrometer-sized powders, knowing their optical properties, like the refractive index, is a useful tool for optoelectronic device applications. For molecular diamondoids, the refractive index increases with decreasing wavelength and increasing polymantane order [60]. Still, the refractive index of the largest diamondoid, **12312HEX** (1.68 at 589 nm), is much lower than that of microscopic diamond (2.42 at 589 nm, Figure 1.12).

Lower diamondoids have low dielectric constants in the range of 2.46 to 2.65, which is significantly lower than that of bulk diamond ($\kappa = 5.66$) or SiO_2 ($\kappa = 4.5$) [61]. This property is postulated to be a consequence of the lower density of diamondoid crystals when compared to, e.g., bulk diamond. Diamondoids therefore have the potential to be used for producing insulating interlayers in nanoelectronic devices.

One of the most fascinating mechanical properties of diamondoid crystals is their resilience in high-pressure environments. This observation is not surprising considering how diamond forms in nature, but it still deserves mentioning in

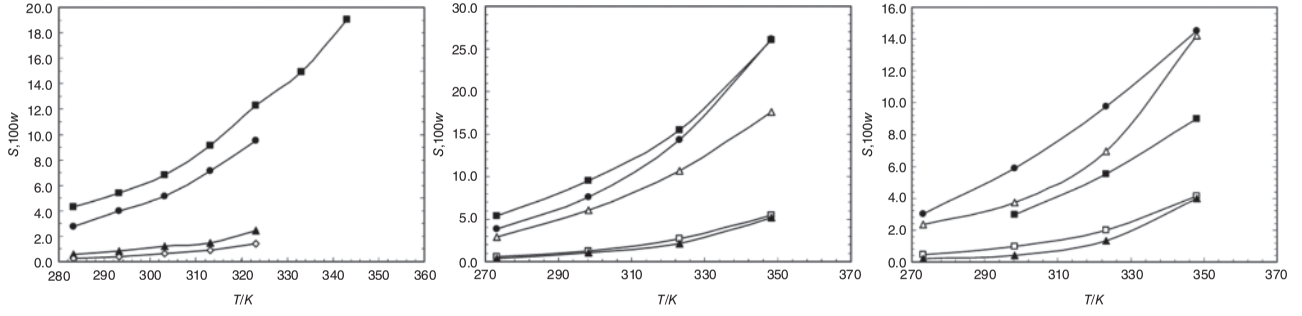

Figure 1.10 Mass fraction solubility (S) of **DIA** (left), **TRIA** (middle), and **121TET** (right) in acetone (▲), ethyl acetate (▲), toluene (●), and cyclohexane (♦) at various temperatures. Source: Reproduced from Ref. [57] with permission from the American Chemical Society, 2008.

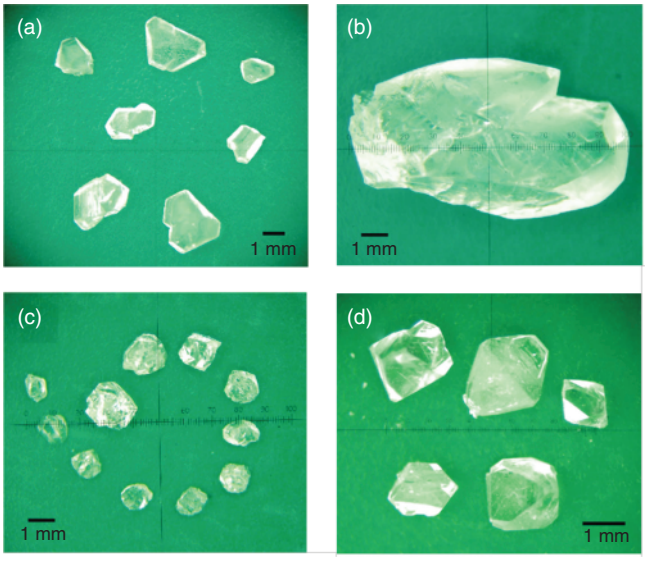

Figure 1.11 Single crystals of **AD** (a,b), **DIA** (c), and **121TET** (d). Source: Reproduced from Ref. [58] with permission from the American Chemical Society, 2010.

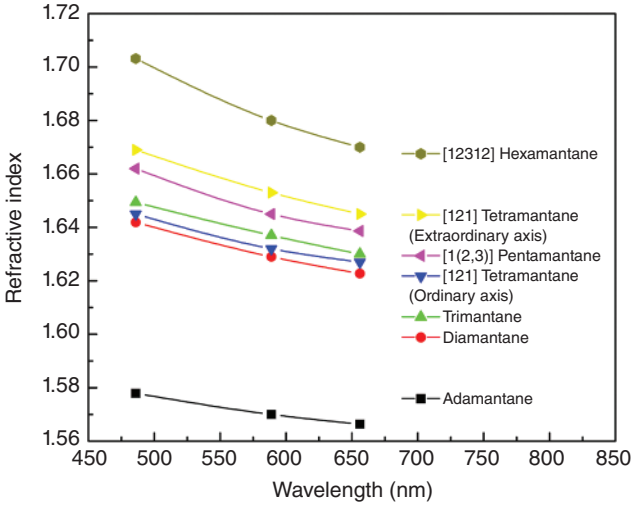

Figure 1.12 Wavelength dependence of refractive index (n) for diamondoids. Source: Reproduced from Ref. [60] with permission from Elsevier, 2008.

the context of their usefulness. Diamondoids at high-pressure conditions readily undergo solid–solid phase transitions without polymerization or decomposition [62]. Such phase transitions can be stimulated by both changes in temperature and/or pressure and often have low energy barriers. For example, **121TET** undergoes a phase transition from the monoclinic $P2_1/n$ structure to a triclinic $P1$ phase starting at pressures of about 13 GPa, and when the pressure is subsequently

released, a new solid phase having the *Pc* space group forms at ambient conditions [63]. Both the starting and the ending solid phases in this process have comparable stability, pointing toward the conservation of the structural motifs upon decompression. This example illustrates that different polymorphs formed after pressurization change only their intermolecular packing, and no degradation of the cage molecules occurs because of their stable diamond-like structure, which is a significant advantage over other types of organic materials. What is more, the molecular geometry of the individual cages also affects the compressibility of the corresponding crystal, making diamondoids of different shapes a rich toolbox of nano-sized building blocks for organic, high-pressure material design.

1.5 Spectroscopy of Diamondoids

The uniqueness of unfunctionalized diamondoids when compared to other hydrocarbons becomes especially apparent when noting their spectroscopic and photophysical properties [61]. Bulk diamond is a good electrical insulator with a large band gap. Luckily, with increasing diamondoid size, the HOMO–LUMO gap decreases and shows a tendency to converge close to the fundamental gap of bulk diamond [64]. For example, larger nanodiamonds with sizes up to 2 nm have computed band gap values of 6.7 eV as compared to 5.5 eV for bulk diamond [65]. Structurally well-defined nanodiamonds display strong quantum confinement effects at particle sizes ranging from 0.5 to at least 2 nm, but it is the size and not the shape of the particles that affect the band gap values. This was demonstrated by the comparison of octahedral vs. tetrahedral nanodiamonds that in the end showed the same trends in band gap narrowing. Since there appears to exist a limit to gap narrowing for nanodiamonds, a proposed method for further reduction of the gap is the introduction of external or internal doping substituents (C—H bond substitution and replacement of cage CH/CH_2 groups, respectively). As will be demonstrated in Chapter 12, doping is a very successful strategy for semiconductor applications of diamondoids. Note that such size-property relationships hold true not only for diamondoids but for parent diamond nanoparticles as well: particle sizes must be around 2 nm to start observing an increase in the optical gap (vide infra) [66]. In other words, reducing the size of bulk diamond to the nanoscale has a pronounced effect on the optical gap of the resulting nanoparticle, with a decrease in the optical gap by increasing nanoparticle size being more rapid for diamond than for, e.g., Si or Ge, where quantum confinement effects persist up to 6–7 nm.

Another computational study on diamondoids found that quantum confinement effects essentially disappear in diamondoid structures larger than 1 nm [67]. However, the applied Monte Carlo computations predict a small exciton binding energy and a negative electron affinity (NEA) for nanodiamonds of that size, which is a consequence of significant LUMO delocalization (Figure 1.13). Note here that the HOMO is predominately localized on the C—C bonds inside the nanoparticle, while the delocalized LUMO has a considerable probability outside of the surface boundaries and is mostly composed of the C—H bonds. With increasing

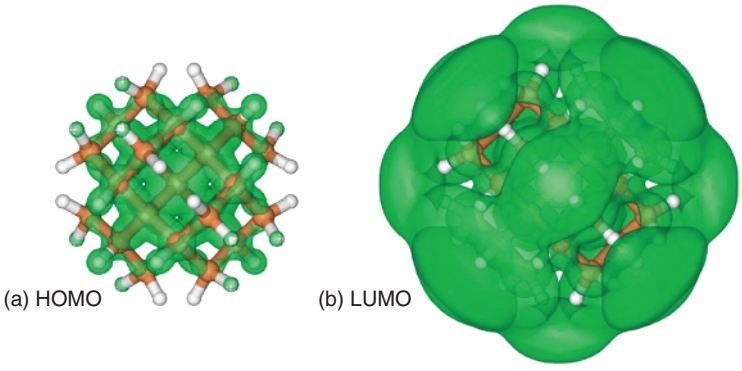

Figure 1.13 Isosurface plots of the square of the (a) HOMO and (b) LUMO of hydrogen-terminated spherical diamond-like nanoparticle $C_{29}H_{36}$. The green isosurfaces include 50% of the charge in each orbital. Source: Reproduced from Ref. [67] with permission from the American Physical Society, 2005.

nanoparticle size, the HOMO ultimately converges to the valence-band maximum of bulk diamond, while the LUMO remains near the surface boundary and does not become a conduction band minimum. Such an almost defect-like nature of the LUMO is the reason why the optical gaps of large diamondoids lie below the gap value of bulk diamond.

As the HOMOs predominately describe the C—C bonding, the vibrational motion of the carbon nuclei has a significant effect on the orbital energies, while the higher-lying orbitals are often Rydberg states that are more sensitive to the vibrational motion of the hydrogen atoms. It follows that in order to reliably compute the optical properties of diamondoids, quantum nuclear dynamics are needed to ensure accurate prediction of their photophysics [68]. Despite such theoretical requirements, recent time-dependent density functional theory (TD-DFT) approaches for vibrationally resolved photoelectron spectra simulations succeeded in coming very close to fully reproducing the experimentally observed vibrational fine structure [69]. What still remains to be tackled in that particular computational approach are errors in computed spectral redshifts upon increasing particle size due to the lack of many-body corrections, a trait that is inherent to the method, as well as the absence of satellites in the high-energy region of the spectra due to electron-nuclear coupling. Further computational studies confirmed that the high diamondoid symmetries lead to forbidden transitions [70]. However, it was also noted that using HOMO–LUMO gaps for the approximation of diamondoid optical gaps was somewhat of an oversimplification, especially since their absorption and emission spectra are vibronically highly structured and often accompanied by broadened and shifted optical bands.

When diamondoids approach the 1 nm range, their crystal morphology itself begins to affect their structural integrity [71]. Theoretical models predicted that while the initial cubic morphology provides relaxation structures comparable to bulk diamond itself, octahedral and cuboctahedral starting materials gradually transform from a pure sp^3 to a mixed sp^3 and sp^2 bonding network, essentially

converting the particle into partially unsaturated layered morphologies. This finding implies that spontaneous phase transitions of nanodiamond clusters starting from the outer carbon atom shells need to be taken into account when designing functional nanodevices. However, hydrogen-terminated diamondoids do not suffer from such layer transformation effects. Dehydrogenated octahedral and cuboctahedral nanodiamond particles up to 1 nm in diameter are therefore structurally unreliable and unstable morphologies that readily undergo partial graphitization and exfoliation of their (111) surfaces, which consequently opens up an important niche for applications. Density functional theory computations up to decamantane confirm this reasoning since hydrogen-terminated diamondoids indeed retain atomic arrangements and electronic structures similar to those of bulk diamond [64].

The computed equilibrium C—C bond lengths and bond angles for diamondoids are comparable to those of bulk diamond, providing them with diamond-like properties, especially as the size of the diamondoids increases. Quantum confinement effects were studied using X-ray absorption spectroscopy, and the resulting diamondoid gas phase spectra (Figure 1.14) show that blueshifts in the band edges do not occur with decreasing particle size, as would be expected for typical group IV semiconductors [72]. In other words, diamondoid clusters display some differences from bulk diamond, which can be advantageous for some applications.

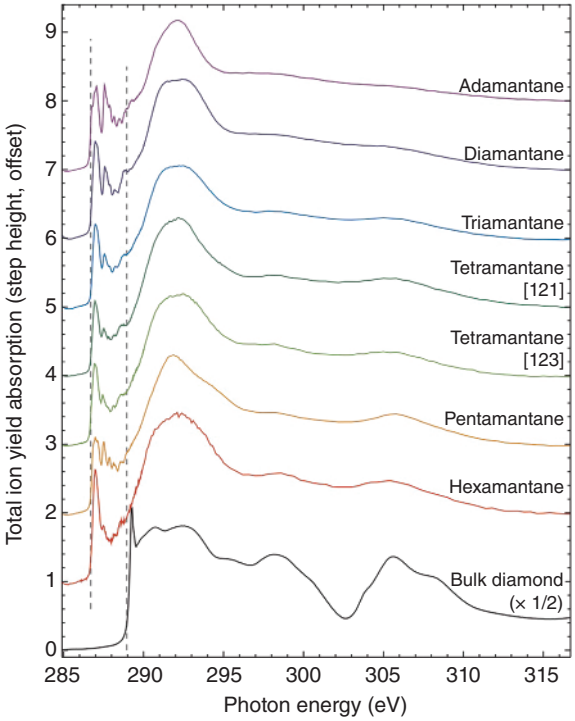

Figure 1.14 Carbon *K*-edge absorptions of selected diamondoids and bulk diamond. Source: Reproduced from Ref. [72] with permission from the American Physical Society, 2005.

While the information on HOMO–LUMO gaps is fundamentally important, the optical gaps (based on symmetry-allowed transitions) provide more relevant information on the properties of diamondoids. The optical gaps of diamondoids measured in the gas phase [73] are in agreement with the experimental and computed trends in changes of the HOMO–LUMO gaps but display strong shape dependence (Figure 1.15) within different topological families (3D, 2D, and 1D denote tetrahedral, prism, and rod-shaped diamondoids, respectively). This is due to the forbidden HOMO → LUMO transitions for some highly symmetric structures. The optical gaps primarily originate from the single-particle transition from HOMO to LUMO or to LUMO+1 and LUMO+2 depending on the selection rule. For instance, **TET** with C_{2h} symmetry (**121TET**) has the first dipole active transition between HOMO and LUMO+2, while HOMO → LUMO transitions are allowed for C_{3v} and C_2 **TET**s. Such symmetry dependence of optical gaps and excitation energy agreed fully with the experiment (Table 1.3).

While the optical gaps of $C_{26}H_{32}$ **1213PENT** (5.75 eV) and bulk diamond display remarkable similarities, the absolute value of 5.5 eV is still unreachable with diamondoids of this size. This agrees well with computations on larger diamondoids that also predict a rapid decrease of the absorption gap (Figure 1.16, left), which becomes similar to the computation for bulk diamond only for particles of about 1 nm in diameter ($C_{87}H_{78}$) [75].

More detailed TD-DFT computations on small diamondoids with the PBE0 method [74b] reveal that the first 3s-like Rydberg excitation is common for all diamondoids (Figure 1.16, right) except for C_{2h}-symmetric **121TET** and **12312HEX,** where such excitations are dipole-forbidden and, therefore, 3*p*-like Rydberg transitions occur instead. For tetrahedral **AD** and **1(2,3)4PENT** both $t_2 \rightarrow a_1(3s)$ and

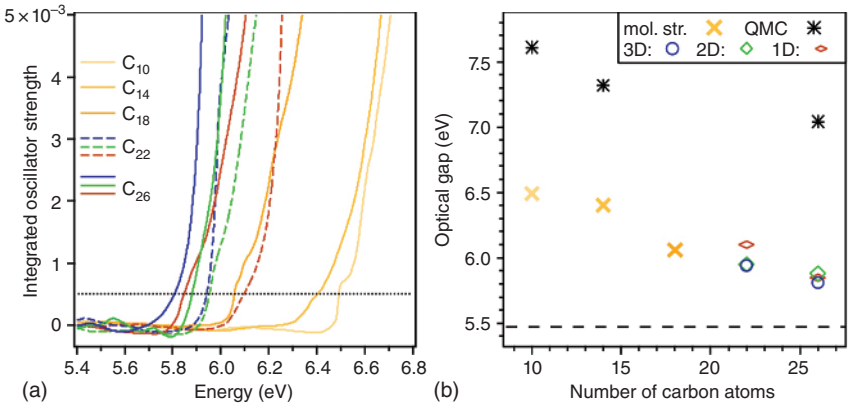

Figure 1.15 (a) Integrated oscillator strength measured for diamondoids **AD** (C_{10}), **DIA** (C_{14}), **TRIA** (C_{18}), as well as for isomeric tetramantanes (C_{22}) and pentamantanes (C_{26}). The threshold defining the optical gap is marked by a dotted line. (b) Experimental optical gaps as a function of size compared to optical gaps derived by quantum Monte Carlo (QMC) calculations. The dashed line marks the energy gap of bulk diamond, and 3D, 2D, and 1D denote tetrahedral, prism, and rod-shaped diamondoids, respectively. Source: Reproduced from Ref. [73] with permission from the American Physical Society, 2009.

Table 1.3 Ground state symmetries, TD-PBE0/aug-cc-pVTZ computed and experimental optical gaps (E_{gap}), and excitation energies of selected diamondoids based on photoluminescence measurements (Source: From [73, 74]).

Diamondoid	Symmetry	Formula	E_{gap} (eV) Comp.	E_{gap} (eV) Exp.	Excitation energy (eV) Exp.
AD	T_d	$C_{10}H_{16}$	6.66	6.49	6.49
DIA	D_{3d}	$C_{14}H_{20}$	6.75	6.40	6.60
TRIA	C_{2v}	$C_{18}H_{24}$	6.12	6.06	6.78
121TET	C_{2h}	$C_{22}H_{28}$	6.25	**6.10**	**6.88**
1(2)3TET	C_{3v}	$C_{22}H_{28}$	6.04	**5.94**	**5.99**
123TET	C_2	$C_{22}H_{28}$	6.01	**5.95**	**5.98**
1(2,3)4PENT	T_d	$C_{26}H_{32}$	5.99	5.81	5.93
12(1)3PENT	C_1	$C_{26}H_{32}$	–	5.83	6.20
1212PENT	C_{2v}	$C_{26}H_{32}$	5.86	5.85	–
1213PENT	C_1	$C_{26}H_{32}$	–	5.75	6.31

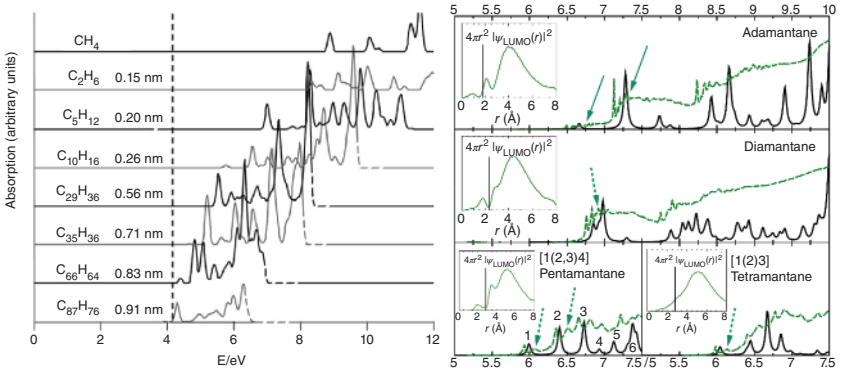

Figure 1.16 *Left*: TD-DFT-computed absorption spectra of diamondoids up to 1 nm in diameter. The vertical dashed line corresponds to the computed absorption gap of bulk diamond. (Source: Reproduced from Ref. [75] with permission from Elsevier, 2005.) *Right*: Computed and experimental absorption spectrum for selected diamondoids. The green (dashed) line shows the experimental spectrum, while the black (continuous) line is the computed spectrum. Inset: radial distribution of 3*s*-like Rydberg state, where vertical line represents the radius of diamondoid. Source: Reproduced from Ref. [74b] with permission from the American Physical Society, 2009.

$t_2 \rightarrow t_2(3p)$ transitions are allowed, but the latter has a higher density of states that leads to a larger absorption for the 3*p*-Rydberg excitation [75].

Diamondoids display intrinsic photoluminescence in the ultraviolet spectral region [76]. For example, **AD** exhibits a quite broad UV luminescence band when photoexcited in the gas phase above its principal optical gap of 6.49 eV (Table 1.3)

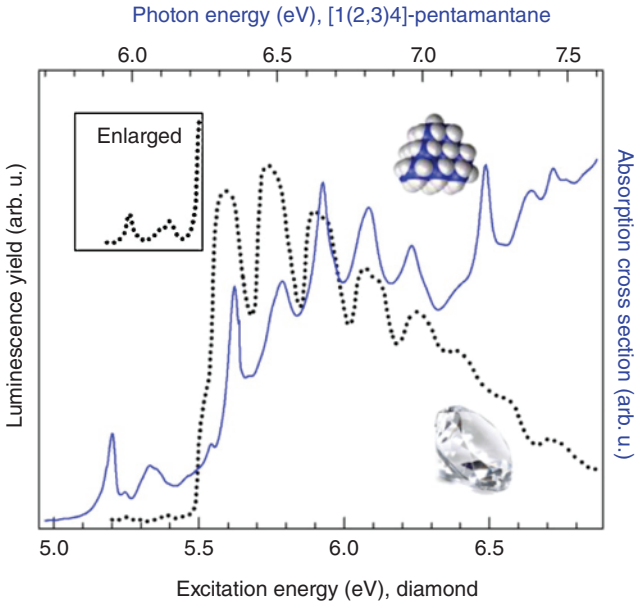

Figure 1.17 Comparison of the optical absorption of **1(2,3)4PENT** (blue line) with the absorption of high-purity type IIa diamond (dotted line). The spectral inset shows the enlarged onset of the bulk diamond spectra. Source: Reproduced from Ref. [73] with permission from the American Physical Society, 2009.

[73]. The optical gap characteristic for diamondoids thus lies in the UV spectral region [77], and the luminescence behavior is attributed to a transition from the delocalized first excited state into different vibrational modes of the electronic ground state [74a]. The majority of such transitions originate from vibrational modes associated with CH wagging and CH_2 twisting of the diamondoid surface atoms (vide infra) [78]. Difficulties in computationally predicting exact lineshapes of diamondoid photoemission spectra arise from electron-vibration coupling that cannot be corrected by applying simple vibration-broadening corrections to the corresponding electronic states [79]. Importantly, the overall optical absorption of diamondoids noticeably changes as a function of their size and shape, and in the case of **1(2,3)4PENT,** the spectrum begins to resemble that of bulk diamond (Figure 1.17). In other words, optical properties change as larger diamondoids are used, demonstrating that diamondoids could form valuable semiconductor nanocrystals for application in light-emitting devices in the deep UV spectral region.

1.6 Ionization Potentials

Since spectral data suggest that diamondoids are also present in space [80], matrix isolation techniques were used to mimic astrophysical conditions. After the deposition of diamondoids in a neon matrix, they were irradiated with high-energy photons, and UV absorption spectra were recorded. This revealed the presence of

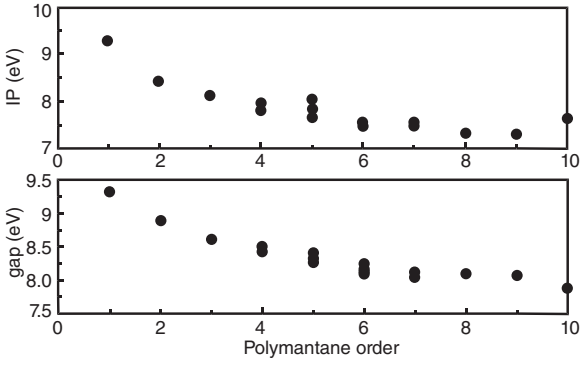

Figure 1.18 Ionization potentials (top) and HOMO–LUMO gaps (bottom) of diamondoids vs. polymantane order. Source: Reproduced from Ref. [83a] with permission from the American Physical Society 2005.

AD and **DIA** cations [81]. However, larger diamondoids starting from **TRIA** could already be ionized by far UV irradiation, and the absorbed energy apparently was distributed through a vibrational mechanism, thereby preventing hydrogen abstraction. An especially fascinating finding was that the spectra obtained from these experiments exhibit noticeable similarities to the spectra obtained from nanodiamonds extracted from the Allende meteorite [82]. We therefore next focus on the diamondoid ionization potentials (IPs) because they are such a fundamentally important property of materials in general. The IPs and HOMO–LUMO gaps decrease with increasing diamondoid order (Figure 1.18) and are well-reproduced by computations [21], but adiabatic IP values are systematically underestimated [67, 83]. Quantitative studies [83b] using total-ion-yield spectroscopy utilizing the commonly used linearization procedure revealed a trend of decreasing adiabatic IP values as a function of diamondoid size, with **AD** having IP = 9.23 eV and going down to 8.07 eV for **1(2,3)4PENT**. In the case of **AD** and cyclohexane as a reference, the agreement with the NIST [84] data is very good. Diamondoids form highly delocalized ionized states whose structures will be discussed in detail in Chapter 4; studying them was attempted by many but is still experimentally challenging.

1.7 Electron Affinities

Alkanes display negative electron affinities (EAs) [85], and the anions derived from saturated hydrocarbons are metastable, where the methane radical anion is the prototype [86]. The experimental observation of the adamantane radical anion ($\mathbf{AD}^{-\cdot}$) was attempted in 1963 [87] but was unsuccessful [88]. The DFT geometry optimization and frequency analysis of the anionic $^2A_1$ state of **AD** [89] display a minimum at T_d symmetry with altering C—C distances in the cage and slightly elongated CH bonds. As only small geometric changes occur upon reduction, the vertical and adiabatic EAs of **AD** are close and range from −1.0 to −0.5 eV [89, 90]. The ultraviolet photoelectron spectroscopy (UPS) spectra of the thick (27 Å) **AD** layer on the Cu(111) surface [91] estimate the EA of solid **AD** as −0.3 eV. The diffusion Monte Carlo simulations [67] predict a negative EA of −0.13 and − 0.26 eV for **AD** and **1(2,3)4PENT**, respectively. The plane-wave DFT computations also

show a negative EA of −0.3 eV for **121TET** [92]. The ability to form highly ordered surface self-assembled monolayers in combination with negative EAs determines the potential of diamondoids for the construction of cold electron emitters and is discussed in detail in Chapter 5.

1.8 Vibrational Spectroscopy

As could be expected from their hydrocarbon nature, infrared spectroscopy of diamondoids produces relatively straightforward absorptions that can be considered a spectral fingerprint of this class of compounds. There exist several general groups of signals corresponding to their vibrational modes: C—H stretching modes around 2900 cm^{-1}, CH_2 scissoring modes (commonly as doublets) around 1450 cm^{-1}, C—H bending and CH_2 rocking, wagging, and twisting modes between 1000 and 1400 cm^{-1}, C—C stretching around 1000 cm^{-1}, and skeletal deformation modes below 1000 cm^{-1} [93]. The existence of such characteristic spectral signals can be used as a means of detection for the presence of diamondoids, for example, in deep space, where nonspectral characterization methods are not applicable [80c]. The computational approaches for evaluating vibrational spectra of diamondoids were found to reproduce the experimental spectral signals well, meaning they can be effectively used for predicting spectra of even higher diamondoids, as was demonstrated in the case of cyclohexamantane [93, 94]. The most characteristic IR bands of higher diamondoids (C—H stretching modes around 2900 cm^{-1} and doublet around 1450 cm^{-1} of CH_2 scissoring modes) are computationally reproduced very well and are almost independent of the basis set [93]. The same is true even for the fingerprint region (1000–1400 cm^{-1}). The experimental Raman spectra have been nearly completely assigned based on comparison with DFT-computed vibrational frequencies and Raman intensities. Each diamondoid produced a unique Raman spectrum (Figure 1.19), which allows for differentiation between the structures. A very good agreement is observed between the experimental [50] and computed [96] vibrational spectra of **12312HEX**.

From the above, it seemed that the experimental absorptions in the CH-stretching region are not very characteristic for the assignment of a diamondoid structure. However, the high-resolution inelastic STM-based IR spectroscopy (IRSTM) of submonolayers of **121TET** and **123TET** on Au(111) enables the distinguishing between the structures clearly (Figure 1.20).

Computations on large (up to 1.92 nm) H-terminated nanodiamond particles show that the major IR peaks in the region of 900–1300 cm^{-1} shift toward high wavenumbers as size increases, while the C—H vibrations in the range show the opposite trend [98].

UV resonance Raman spectroscopy has been used to characterize **DIA** *syn*- and *anti*-dimers that contain a central C—C double bond [99], and it was found that their observed Raman resonance energies were significantly lower than the HOMO–LUMO gaps of the corresponding unmodified diamondoids. Thus, compound screening when modifying the optical gap in diamondoids by functional

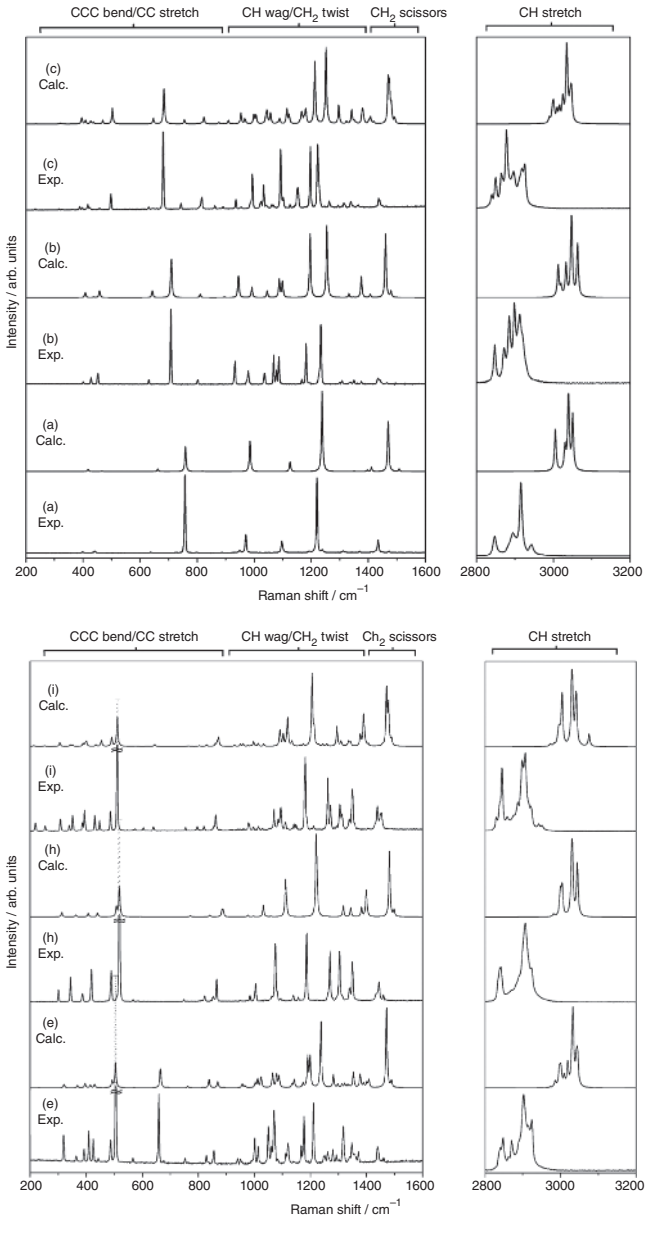

Figure 1.19 *Top*: Experimental and computed Raman spectra (from bottom) for (a) **AD**, (b) **DIA**, (c) and **TRIA**. *Bottom*: Experimental and computed spectra (from bottom) for (e) **1(2)3TRIA**, (h) **1(2,3)4PENT**, and (i) 3-methyl-**1(2,3)4PENT**. Source: Reproduced from Ref. [95] with permission from Elsevier, 2006.

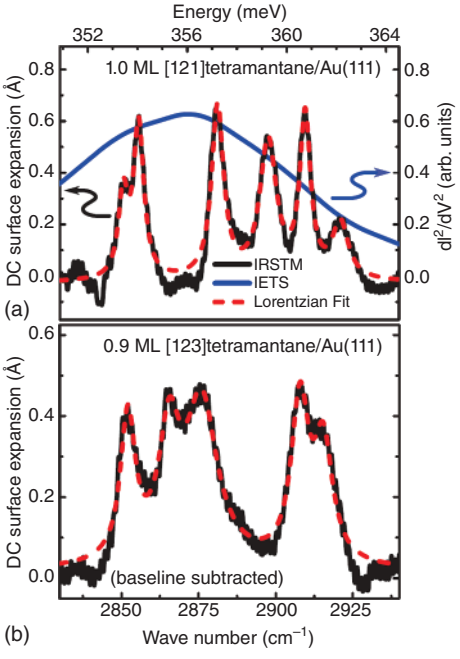

Figure 1.20 Molecular IR absorption of **121TET** (top) and **123TET** (bottom) deposited on Au(111) surface. The blue line shows the unresolved broad peak from STM inelastic electron tunneling spectroscopy (IETS) measurements. Source: Reproduced from Ref. [97] with permission from the American Physical Society, 2013.

group introduction (so-called "doping" that will be discussed in detail in Chapter 12) can be performed using readily available Raman spectroscopy. In a subsequent study, diamondoid dimers and trimers connected with either a single or a double C—C bond and consisting of combinations of **AD** and **DIA** cages were characterized with valence photoelectron spectroscopy [100]. When a double bond is present in the molecule, it significantly impacts the electronic structure of the HOMO, in contrast to molecules with connecting single bonds, where the impact is only small. Moreover, the orbital superposition of both cages in the singly bonded particles determines the overall electronic structure of such systems. This combination of orbitals directly influences the ionization potentials, as homo-dimers have IP values below those of the corresponding monomers, and the measured IPs for hetero-dimers strongly depend on particle composition. Composite diamondoids like **DIA** dimers can also form van der Waals crystals, and it was confirmed that the central double bond predominately influences optical properties both in the gas phase, where single molecules are observed, and in the crystalline solid state [101]. Note that optical band gaps in such systems are significantly lowered (by 0.5–1.0 eV) when compared to their saturated analogues.

As we have seen, diamondoids underwent much turbulence in the course of their history. They evolved from being structural curiosities isolated from oil to inspiring target molecules that challenged the limits of synthetic organic chemistry, to becoming multi-gram resources available from nature and useful for medicine, and finally, to affording modern-day applicability as unique building blocks in nanomaterial design. It is satisfying to see that this fascinating class of compounds went full circle: it was first found in and today is efficiently extracted from oil deposits.

Although our main goal is to demonstrate a wide range of chemical transformations feasible on diamondoids and showcase the fascinating properties of the prepared derivatives and nanostructures, it is still good to pause for a moment and admire the simple beauty of these highly symmetrical jewels of nature.

References

1 Decker, H. (1924). Wege zur Synthese des Diamanten. *Z. Angew. Chem.* 37: 795.
2 Schreiner, P.R., Fokin, A.A., Reisenauer, H.P. et al. (2009). [123]Tetramantane: parent of a new family of sigma-helicenes. *J. Am. Chem. Soc.* 131: 11292–11293.
3 Balaban, A.T. and Schleyer, P.v.R. (1978). Systematic classification and nomenclature of diamond hydrocarbons-I: graph-theoretical enumeration of polymantanes. *Tetrahedron* 34: 3599–3609.
4 (a) Shenderova, O.A., Zhirnov, V.V., and Brenner, D.W. (2002). Carbon nanostructures. *Crit. Rev. Solid State Mater. Sci.* 27: 227–356. (b) Mochalin, V.N., Shenderova, O., Ho, D., and Gogotsi, Y. (2012). The properties and applications of nanodiamonds. *Nat. Nanotechnol.* 7: 11–23.
5 Fokin, A.A., Tkachenko, B.A., Fokina, N.A. et al. (2009). Reactivities of the prism-shaped diamondoids [1(2)3]tetramantane and [12312]hexamantane (Cyclohexamantane). *Chem. Eur. J.* 15: 3851–3862.
6 Eckroth, D.R. (1967). A method for manual generation of correct von Baeyer names of polycyclic hydrocarbons. *J. Org. Chem.* 32: 3362–3365.
7 (a) Balaban, A.T. (2012). Partitioned-formula periodic tables for diamond hydrocarbons (diamondoids). *J. Chem. Inf. Model.* 52: 2856–2863. (b) Balaban, A.T. (2013). Diamond hydrocarbons and related structures. In: *Diamond and Related Nanostructures* (ed. M.V. Diudea and C.L. Nagy), 1–27. Dordrecht: Springer Netherlands. (c) Balaban, A.T. and Rucker, C. (2013). How to specify the structure of substituted blade-like zigzag diamondoids. *Cent. Eur. J. Chem.* 11: 1423–1430.
8 Cupas, C., Schleyer, P.v.R., and Trecker, D.J. (1965). Congressane. *J. Am. Chem. Soc.* 87: 917–918.
9 Balaban, A.T. (2013). Diamond hydrocarbons revisited: partitioned formula tables of diamondoids. *J. Math. Chem.* 51: 1043–1055.
10 Wang, Y.T., Zhao, Y.J., Liao, J.H., and Yang, X.B. (2018). Theoretical investigations on diamondoids (C_nH_m, n=10–41): nomenclature, structural stabilities, and gap distributions. *J. Chem. Phys.* 148: 014306.
11 Willey, T.M., Lee, J.R.I., Brehmer, D. et al. (2021). X-ray spectroscopic identification of strain and structure-based resonances in a series of saturated carbon-cage molecules: Adamantane, twistane, octahedrane, and cubane. *J. Vac. Sci. Technol. A* 39: 053208.
12 Engler, E.M., Andose, J.D., and Schleyer, P.v.R. (1973). Critical evaluation of molecular mechanics. *J. Am. Chem. Soc.* 95: 8005–8025.
13 Schleyer, P.v.R., Williams, J.E., and Blanchard, K.R. (1970). Evaluation of strain in hydrocarbons. The strain in adamantane and its origin. *J. Am. Chem. Soc.* 92: 2377–2386.

14 (a) Pitzer, K.S. (1955). London force contributions to bond energies. *J. Chem. Phys.* 23: 1735–1735. (b) Pitzer, K.S. and Catalano, E. (1956). Electronic correlation in molecules III. The paraffin hydrocarbons. *J. Am. Chem. Soc.* 78: 4844–4846.

15 Wodrich, M.D., Wannere, C.S., Mo, Y. et al. (2007). The concept of protobranching and its many paradigm shifting implications for energy evaluations. *Chem. Eur. J.* 13: 7731–7744.

16 Joyce, J.P., Shores, M.P., and Rappe, A.K. (2020). Protobranching as repulsion-induced attraction: a prototype for geminal stabilization. *Phys. Chem. Chem. Phys.* 22: 16998–17006.

17 Dorofeeva, O.V. and Ryzhova, O.N. (2019). Enthalpies of formation of diamantanes in the gas and crystalline phase: comparison of theory and experiment. *Struct. Chem.* 30: 615–621.

18 Rablen, P.R. (2020). A procedure for computing hydrocarbon strain energies using computational group equivalents, with application to 66 molecules. *Chemistry* 2: 347–360.

19 Wheeler, S.E., Houk, K.N., Schleyer, P.v.R., and Allen, W.D. (2009). A hierarchy of homodesmotic reactions for thermochemistry. *J. Am. Chem. Soc.* 131: 2547–2560.

20 (a) Gronert, S. (2009). The folly of protobranching: turning repulsive interactions into attractive ones and rewriting the strain/stabilization energies of organic chemistry. *Chem. Eur. J.* 15: 5372–5382. (b) Kemnitz, C.R. (2013). Electron delocalization explains much of the branching and protobranching stability. *Chem. Eur. J.* 19: 11093–11095.

21 Fokin, A.A., Tkachenko, B.A., Gunchenko, P.A. et al. (2005). Functionalized nanodiamonds Part I. An experimental assessment of diamantane and computational predictions for higher diamondoids. *Chem. Eur. J.* 11: 7091–7101.

22 Bondi, A. (1964). van der Waals volumes and radii. *J. Phys. Chem.* 68: 441–451.

23 Böttger, O. (1937). Über einige organische Verbindungen "diamantoider" Struktur. *Ber. Dtsch. Chem. Ges.* 70: 314–325.

24 Prelog, V. and Seiwerth, R. (1941). Über die Synthese des Adamantans. *Chem. Ber.* 1644–1648.

25 Meerwein, H., Kiel, F., Klösgen, G., and Schoch, E. (1922). Über bicyclische und polycyclische Verbindungen mit Brückenbindung. Über das Bicyclo-[1,3,3]-nonan und seine Abkömmlinge. *J. Prakt. Chem.* 104: 161–206.

26 Seiwerth, R. (1996). Prelog's Zagreb school of organic chemistry (1935–1945). *Croat. Chem. Acta* 69: 379–397.

27 Meerwein, H. and Schürmann, W. (1913). Über eine Synthese von Abkömmlingen des Bicyclo-[1,3,3]-nonans. *Liebigs Ann.* 398: 196–242.

28 Prelog, V. and Seiwerth, R. (1941). Über eine neue, ergiebigere Darstellung des Adamantans. *Ber. Bunsen. Phys. Chem* 1769–1772.

29 Stetter, H., Bänder, O.E., and Neumann, W. (1956). Über Verbindungen mit Urotropin-Struktur, VIII. Mitteil: Neue Wege der Adamantan-Synthese. *Chem. Ber.* 89: 1922–1926.

30 Schleyer, P.v.R. (1957). A simple preparation of adamantane. *J. Am. Chem. Soc.* 79: 3292.

31 Schleyer, P.v.R., Donaldson, M.M., Nicholas, R.D., and Cupas, C. (1962). Adamantane (tricyclo[3.3.1.$1^{3,7}$]decane). *Org. Synth.* 42: 8.

32 Fort, R.C. and Schleyer, P.v.R. (1964). Adamantane: consequences of the diamondoid structure. *Chem. Rev.* 64: 277–300.

33 Schleyer, P.v.R. and Streitwieser, A. (2015). *From the Ivy League to the Honey Pot, The Foundations of Physical Organic Chemistry: Fifty Years of the James Flack Norris Award*, 169–198. Washington, DC: ACS Symposium Series, American Chemical Society.

34 Karle, I.L. and Karle, J. (1965). Crystal and molecular structure of congressane $C_{14}H_{20}$ by X-ray diffraction. *J. Am. Chem. Soc.* 87: 918–920.

35 Gund, T.M., Williams, V.Z., Osawa, E., and Schleyer, P.v.R. (1970). A convenient, high-yield preparation of diamantane (congressane). *Tetrahedron Lett.* 3877–3880.

36 Gund, T.M., Osawa, E., Williams, V.Z. et al. (1974). Preparation of diamantane. Physical and spectral properties. *J. Org. Chem.* 39: 2979–2987.

37 Gund, T.M., Thielecke, W., and Schleyer, P.v.R. (1973). Diamantane - pentacyclo[7.3.1.1^{4,12}.0^{2,7}.0^{6,11}]tetradecane (butanetetraylnaphthalene, 3,5,1,7-1,2,3,4- decahydro). *Org. Synth.* 53: 30–33.

38 Williams, V.Z., Schleyer, P.v.R., Gleicher, G.J., and Rodewald, L.B. (1966). Triamantane. *J. Am. Chem. Soc.* 88: 3862–3863.

39 Burns, W., McKervey, M.A., and Rooney, J.J. (1975). New synthesis of triamantane involving a novel rearrangement of a polycyclic olefin in the gas phase on platinum. *J. Chem. Soc. Chem. Commun.* 965–966.

40 (a) Hamilton, R., McKervey, M.A., Rooney, J.J. et al. (1976). A short synthesis of triamantane. *J. Chem. Soc. Chem. Commun.* 1027–1028. (b) Hollowood, F.S., McKervey, M.A., Hamilton, R., and Rooney, J.J. (1980). Synthesis of triamantane. *J. Org. Chem.* 45: 4954–4958.

41 Osawa, E., Furusaki, A., Hashiba, N. et al. (1980). Thermodynamic rearrangements of larger polycyclic hydrocarbons derived from the 38.5 and 41.5 °C melting dimers of cyclooctatetraene. Crystal and molecular structures of 5-bromoheptacyclo[8.6.0.0^{2,8}.0^{3,13}.0^{4,11}.0^{5,9}.0^{12,16}]hexadecane (5-bromo-[C_2]-bisethanobisnordiamantane), 6,12-dibromoheptacyclo[7.7.0.0^{2,6}.0^{3,15}.0^{4,12}.0^{5,10}.0^{11,16}]hexadecane, and nonacyclo[11.7.1.1^{2,18}.0^{3,16},0^{4,13}.0^{5,10}.0^{6,14}.0^{7,11}.0^{15,20}]docosane (bastardane). *J. Org. Chem.* 45: 2985–2995.

42 Burns, W., Mitchell, T.R.B., McKervey, M.A. et al. (1976). Synthesis and crystal structure of anti- tetramantane, a large diamondoid fragment. *J. Chem. Soc. Chem. Commun.* 893–895.

43 Roberts, P.J. and Ferguson, G. (1977). *anti*-Tetramantane, a large diamondoid fragment. *Acta Crystallogr. B* 33: 2335–2337.

44 Burns, W., McKervey, M.A., Mitchell, T.R.B., and Rooney, J.J. (1978). A new approach to the construction of diamondoid hydrocarbons. Synthesis of *anti*-tetramantane. *J. Am. Chem. Soc.* 100: 906–911.

45 (a) Schwertfeger, H., Fokin, A.A., and Schreiner, P.R. (2008). Diamonds are a chemist's best friend: Diamondoid chemistry beyond adamantane. *Angew. Chem. Int. Ed.* 47: 1022–1036. (b) McKervey, M.A. (1980). Synthetic approaches to large diamondoid hydrocarbons. *Tetrahedron* 36: 971–992.

46 Hopf, H. (2003). Diamonds from crude oil? *Angew. Chem. Int. Ed.* 42: 2000–2002.

47 Landa, S. and Macháček, V. (1933). Sur l'adamantane, nouvel hydrocarbure extrait du naphte *Collect*. *Czech. Chem. Commun.* 5: 1–5.

48 Dahl, J.E., Moldowan, J.M., Peters, K.E. et al. (1999). Diamondoid hydrocarbons as indicators of natural oil cracking. *Nature* 399: 54–57.

49 Dahl, J.E., Liu, S.G., and Carlson, R.M.K. (2003). Isolation and structure of higher diamondoids, nanometer-sized diamond molecules. *Science* 299: 96–99.

50 Dahl, J.E.P., Moldowan, J.M., Peakman, T.M. et al. (2003). Isolation and structural proof of the large diamond molecule, cyclohexamantane ($C_{26}H_{30}$). *Angew. Chem. Int. Ed.* 42: 2040–2044.

51 Hala, S., Landa, S., and Hanus, V. (1966). Isolation of tetracyclo[6.3.1.$0^{2,6}$.$0^{5,10}$]dodecane and pentacyclo[7.3.1.$1^{4,12}$.$0^{2,7}$.$0^{6,11}$]tetradecane (diamantane) from petroleum. *Angew. Chem. Int. Ed.* 5: 1045–1046.

52 Dahl, J.E.P., Moldowan, J.M., Wei, Z. et al. (2010). Synthesis of higher diamondoids and implications for their formation in petroleum. *Angew. Chem. Int. Ed.* 49: 9881–9885.

53 (a) Stauss, S., Miyazoe, H., Shizuno, T. et al. (2010). Synthesis of the higher-order diamondoid hexamantane using low-temperature plasmas generated in supercritical xenon. *Jpn. J. Appl. Phys.* 49: 070213. (b) Shizuno, T., Miyazoe, H., Saito, K. et al. (2011). Synthesis of diamondoids by supercritical xenon discharge plasma. *Jpn. J. Appl. Phys.* 50: 030207. (c) Oshima, F., Stauss, S., Ishii, C. et al. (2012). Plasma microreactor in supercritical xenon and its application to diamondoid synthesis. *J. Phys. D* 45: 402003. (d) Oshima, F., Stauss, S., Inose, Y., and Terashima, K. (2014). Synthesis and investigation of reaction mechanisms of diamondoids produced using plasmas generated inside microcapillaries in supercritical xenon. *Jpn. J. Appl. Phys.* 53: 010214. (e) Ishii, C., Stauss, S., Kuribara, K. et al. (2015). Atmospheric pressure synthesis of diamondoids by plasmas generated inside a microfluidic reactor. *Diamond Relat. Mater.* 59: 40–46.

54 Nakahara, S., Stauss, S., Kato, T. et al. (2011). Synthesis of higher diamondoids by pulsed laser ablation plasmas in supercritical CO_2. *J. Appl. Phys.* 109: 123304.

55 Stauss, S. and Terashima, K. (2016). *Diamondoids: Synthesis, Properties, and Applications*. Jenny Stanford Publishing p. 242.

56 Bamberg, M., Bursch, M., Hansen, A. et al. (2021). $[Cl@Si_{20}H_{20}]^-$: Parent siladodecahedrane with endohedral chloride ion. *J. Am. Chem. Soc.* 143: 10865–10871.

57 Chan, Y.C., Choy, K.K.H., Chan, A.H.C. et al. (2008). Solubility of diamantane, trimantane, tetramantane, and their derivatives in organic solvents. *J. Chem. Eng. Data* 53: 1767–1771.

58 Iwasa, A., Clay, W.A., Dahl, J.E. et al. (2010). Environmentally friendly refining of diamond-molecules via the growth of large single crystals. *Cryst. Growth Des.* 10: 870–873.

59 Filik, J. (2010). Diamondoid hydrocarbons. In: *Carbon Based Nanomaterials*, vol. 65–66 (ed. N. Ali, A. Ochsner, and W. Ahmed), 1–26.

60 Choi, J.H., Eichele, C., Lin, Y.C. et al. (2008). Determination of effective refractive index of molecular diamondoids by Becke line method. *Scr. Mater.* 58: 413–416.

61 Clay, W.A., Sasagawa, T., Kelly, M. et al. (2008). Diamondoids as low-kappa dielectric materials. *Appl. Phys. Lett.* 93: 172901.

62 Yang, F., Lin, Y., Baldini, M. et al. (2016). Effects of molecular geometry on the properties of compressed diamondoid crystals. *J. Phys. Chem. Lett.* 7: 4641–4647.

63 Yang, F., Lin, Y., Dahl, J.E.P. et al. (2014). High pressure Raman and X-ray diffraction study of [121]tetramantane. *J. Phys. Chem. C* 118: 7683–7689.

64 McIntosh, G.C., Yoon, M., Berber, S., and Tomanek, D. (2004). Diamond fragments as building blocks of functional nanostructures. *Phys. Rev. B* 70: 045401.

65 Fokin, A.A. and Schreiner, P.R. (2009). Band gap tuning in nanodiamonds: first principle computational studies. *Mol. Phys.* 107: 823–830.

66 Raty, J.Y., Galli, G., Bostedt, C. et al. (2003). Quantum confinement and fullerenelike surface reconstructions in nanodiamonds. *Phys. Rev. Lett.* 90: 037401.

67 Drummond, N.D., Williamson, A.J., Needs, R.J., and Galli, G. (2005). Electron emission from diamondoids: a diffusion quantum Monte Carlo study. *Phys. Rev. Lett.* 95: 096801.

68 (a) Patrick, C.E. and Giustino, F. (2013). Quantum nuclear dynamics in the photophysics of diamondoids. *Nat. Commun.* 4: 1–7. (b) Demjan, T., Voros, M., Palummo, M., and Gali, A. (2014). Electronic and optical properties of pure and modified diamondoids studied by many-body perturbation theory and time-dependent density functional theory. *J. Chem. Phys.* 141: 064308.

69 Xiong, T., Wlodarczyk, R., Gallandi, L. et al. (2018). Vibrationally resolved photoelectron spectra of lower diamondoids: a time-dependent approach. *J. Chem. Phys.* 148: 044310.

70 Banerjee, S. and Saalfrank, P. (2014). Vibrationally resolved absorption, emission and resonance Raman spectra of diamondoids: a study based on time-dependent correlation functions. *Phys. Chem. Chem. Phys.* 16: 144–158.

71 Barnard, A.S., Russo, S.P., and Snook, I.K. (2003). Structural relaxation and relative stability of nanodiamond morphologies. *Diamond Relat. Mater.* 12: 1867–1872.

72 Willey, T.M., Bostedt, C., van Buuren, T. et al. (2005). Molecular limits to the quantum confinement model in diamond clusters. *Phys. Rev. Lett.* 95: 113401.

73 Landt, L., Kluender, K., Dahl, J.E. et al. (2009). Optical response of diamond nanocrystals as a function of particle size, shape, and symmetry. *Phys. Rev. Lett.* 103: 047402.

74 (a) Richter, R., Wolter, D., Zimmermann, T. et al. (2014). Size and shape dependent photoluminescence and excited state decay rates of diamondoids. *Phys.*

Chem. Chem. Phys. 16: 3070–3076. (b) Voros, M. and Gali, A. (2009). Optical absorption of diamond nanocrystals from *ab initio* density-functional calculations. *Phys. Rev. B* 80: 161411.

75 Raty, J.Y. and Galli, G. (2005). Optical properties and structure of nanodiamonds. *J. Electroanal. Chem.* 584: 9–12.

76 Landt, L., Kielich, W., Wolter, D. et al. (2009). Intrinsic photoluminescence of adamantane in the ultraviolet spectral region. *Phys. Rev. B* 80: 205323.

77 Voros, M., Demjen, T., Szilvasi, T., and Gali, A. (2012). Tuning the optical gap of nanometer-size diamond cages by sulfurization: a time-dependent density functional study. *Phys. Rev. Lett.* 108: 267401.

78 Richter, R., Rohr, M.I.S., Zimmermann, T. et al. (2015). Laser-induced fluorescence of free diamondoid molecules. *Phys. Chem. Chem. Phys.* 17: 4739–4749.

79 Gali, A., Demjan, T., Voros, M. et al. (2016). Electron-vibration coupling induced renormalization in the photoemission spectrum of diamondoids. *Nat. Commun.* 7: 11327.

80 (a) Bilalbegović, G., Maksimović, A., and Valencic, L.A. (2018). Tetrahedral hydrocarbon nanoparticles in space: X-ray spectra. *Mon. Not. R. Astron. Soc.* 476: 5358–5364. (b) Bauschlicher, C.W., Liu, Y.F., Ricca, A. et al. (2007). Electronic and vibrational spectroscopy of diamondoids and the interstellar infrared bands between 3.35 and 3.55 μm. *Astrophys. J.* 671: 458–469. (c) Pirali, O., Vervloet, M., Dahl, J.E. et al. (2007). Infrared spectroscopy of diamondoid molecules: new insights into the presence of nanodiamonds in the interstellar medium. *Astrophys. J.* 661: 919–925. (d) Bouwman, J., Horst, S., and Oomens, J. (2018). Spectroscopic characterization of the product ions formed by electron ionization of adamantane. *ChemPhysChem* 19: 3211–3218. (e) Greaves, J.S., Scaife, A.M.M., Frayer, D.T. et al. (2018). Anomalous microwave emission from spinning nanodiamonds around stars. *Nat. Astron.* 2: 662–667.

81 Steglich, M., Huisken, F., Dahl, J.E. et al. (2011). Electronic spectroscopy of FUV-irradiated diamondoids: a combined experimental and theoretical study. *Astrophys. J.* 729: 91.

82 Mutschke, H., Andersen, A.C., Jager, C. et al. (2004). Optical data of meteoritic nano-diamonds from far-ultraviolet to far-infrared wavelengths. *Astron. Astrophys.* 423: 983–993.

83 (a) Lu, A.J., Pan, B.C., and Han, J.G. (2005). Electronic and vibrational properties of diamondlike hydrocarbons. *Phys. Rev. B* 72: 035447. (b) Lenzke, K., Landt, L., Hoener, M. et al. (2007). Experimental determination of the ionization potentials of the first five members of the nanodiamond series. *J. Chem. Phys.* 127: 084320.

84 National Institute of Standard, *NIST Chemistry webbook*. http://webbook.nist.gov/chemistry.

85 Meunier, M., Quirke, N., and Binesti, D. (1999). The calculation of the electron affinity of atoms and molecules. *Mol. Simul.* 23: 109–125.

86 de Urquijo, J., Arriaga, C.A., Cisneros, C., and Alvarez, I. (1999). A time-resolved study of ionization, electron attachment and positive-ion drift in methane. *J. Phys. D* 32: 41–45.

87 Bowers, K.W., Greene, F.D., and Nolfi, G.J. (1963). Radical anions of adamantane and hexamethylenetetramine. *J. Am. Chem. Soc.* 85: 3707.

88 Jones, M.T. (1966). The reported adamantane anion radical. Its relationship to benzene anion radical. *J. Am. Chem. Soc.* 88: 174–176.

89 Li, Q.S., Feng, X.J., Xie, Y., and Schaefer, H.F. (2005). Perfluoroadamantane and its negative ion. *J. Phys. Chem. A* 109: 1454–1457.

90 Irikura, K.K. (2008). Sigma stellation: a design strategy for electron boxes. *J. Phys. Chem. A* 112: 983–988.

91 Li, J.R., Niesner, D., and Fauster, T. (2021). Negative electron affinity of adamantane on Cu(111). *J. Phys. Condens. Matter* 33: 135001.

92 Wang, Y., Kioupakis, E., Lu, X. et al. (2008). Spatially resolved electronic and vibronic properties of single diamondoid molecules. *Nat. Mater.* 7: 38–42.

93 Oomens, J., Polfer, N., Pirali, O. et al. (2006). Infrared spectroscopic investigation of higher diamondoids. *J. Mol. Spectrosc.* 238: 158–167.

94 Richardson, S.L., Baruah, T., Mehl, M.J., and Pederson, M.R. (2006). Cyclohexamantane ($C_{26}H_{30}$): first-principles DFT study of a novel diamondoid molecule. *Diamond Relat. Mater.* 15: 707–710.

95 Filik, J., Harvey, J.N., Allan, N.L. et al. (2006). Raman spectroscopy of diamondoids. *Spectrochim. Acta A Mol. Biomol. Spectrosc.* 64: 681–692.

96 Richardson, S.L., Baruah, T., Mehl, M.J., and Pederson, M.R. (2005). Theoretical confirmation of the experimental Raman spectra of the lower-order diamondoid molecule: cyclohexamantane ($C_{26}H_{30}$). *Chem. Phys. Lett.* 403: 83–88.

97 Pechenezhskiy, I.V., Hong, X., Nguyen, G.D. et al. (2013). Infrared spectroscopy of molecular submonolayers on surfaces by infrared scanning tunneling microscopy: Tetramantane on Au(111). *Phys. Rev. Lett.* 111: 126101.

98 Zhuang, C.Q., Jiang, X., Zhao, J.J.J. et al. (2009). Infrared spectra of hydrogenated nanodiamonds by first-principles simulations. *Phys. E: Low-Dimens. Syst. Nanostructures* 41: 1427–1432.

99 Meinke, R., Richter, R., Merli, A. et al. (2014). UV resonance Raman analysis of trishomocubane and diamondoid dimers. *J. Chem. Phys.* 140: 034309.

100 Zimmermann, T., Richter, R., Knecht, A. et al. (2013). Exploring covalently bonded diamondoid particles with valence photoelectron spectroscopy. *J. Chem. Phys.* 139: 084310.

101 Tyborski, C., Meinke, R., Gillen, R. et al. (2017). From isolated diamondoids to a van-der-Waals crystal: a theoretical and experimental analysis of a trishomocubane and a diamantane dimer in the gas and solid phase. *J. Chem. Phys.* 147: 044303.